

Toward Highly Stable Electrocatalysts via Nanoparticle Pore Confinement

Carolina Galeano,^{†,‡} Josef C. Meier,^{§,||,‡} Volker Peinecke,[⊥] Hans Bongard,[†] Ioannis Katsounaros,[§] Angel A. Topalov,^{§,||} Anhui Lu,[⊗] Karl J. J. Mayrhofer,^{*,§} and Ferdi Schüth^{*,†}

[†]Department of Heterogeneous Catalysis, Max-Planck-Institut für Kohlenforschung, Kaiser-Wilhelm-Platz 1, 45470 Mülheim an der Ruhr, Germany

[§]Department of Interface Chemistry and Surface Engineering, Max-Planck-Institut für Eisenforschung GmbH, Max-Planck-Strasse 1, 40237 Düsseldorf, Germany

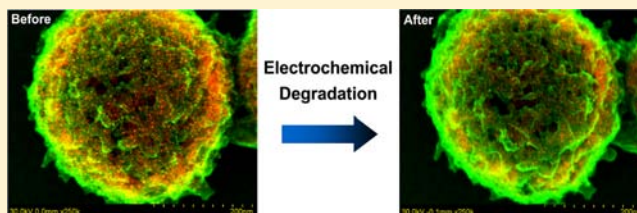
^{||}Center for Electrochemical Sciences, Ruhr-Universität Bochum, Universitätsstrasse 150, 44780 Bochum, Germany

[⊥]The Fuel Cell Research Center ZBT GmbH, Carl-Benz-Straße 201, 47057 Duisburg, Germany

[⊗]State Key Laboratory of Fine Chemicals, Dalian University of Technology, Linggong Road No.2, Dalian 116024, P.R. China

Supporting Information

ABSTRACT: The durability of electrode materials is a limiting parameter for many electrochemical energy conversion systems. In particular, electrocatalysts for the essential oxygen reduction reaction (ORR) present some of the most challenging instability issues shortening their practical lifetime. Here, we report a mesostructured graphitic carbon support, Hollow Graphitic Spheres (HGS) with a specific surface area exceeding $1000 \text{ m}^2 \text{ g}^{-1}$ and precisely controlled pore structure, that was specifically developed to overcome the long-term catalyst degradation, while still sustaining high activity. The synthetic pathway leads to platinum nanoparticles of approximately 3 to 4 nm size encapsulated in the HGS pore structure that are stable at $850 \text{ }^\circ\text{C}$ and, more importantly, during simulated accelerated electrochemical aging. Moreover, the high stability of the cathode electrocatalyst is also retained in a fully assembled polymer electrolyte membrane fuel cell (PEMFC). Identical location scanning and scanning transmission electron microscopy (IL-SEM and IL-STEM) conclusively proved that during electrochemical cycling the encapsulation significantly suppresses detachment and agglomeration of Pt nanoparticles, two of the major degradation mechanisms in fuel cell catalysts of this particle size. Thus, beyond providing an improved electrocatalyst, this study describes the blueprint for targeted improvement of fuel cell catalysts by design of the carbon support.



INTRODUCTION

Electrochemical energy conversion and storage devices, such as batteries, supercapacitors, or fuel cells, will be key elements of future energy systems. Crucial components in all of these devices are the electrodes, where the electrochemical reactions take place. The kinetics of these reactions account for the power density and the energy efficiency of the system, while the electrochemical stability of the electrode materials determines the lifetime of the devices.^{1,2} The oxygen reduction reaction (ORR) plays a decisive role in many electrochemical applications such as, for instance, low temperature polymer electrolyte membrane (PEM) fuel cells or metal–air batteries. Despite its importance, however, it still imposes substantial fundamental and practical challenges. The sluggish kinetics, on the one hand, demand high loading of active Pt-based catalysts, which unfavorably increases the cost of such systems. Considerable improvements in activity have been achieved over recent years by alloying Pt with transition metals as well as by exploring nonprecious metal catalyst concepts.^{3–7} On the other hand, the poor long-term stability of standard and advanced ORR electrocatalysts under the corrosive operating

conditions is remaining a major obstacle.^{8,9} Thus, if electrochemical energy conversion systems shall be introduced on a large scale, the state of the art electrocatalysts will require significant improvements in durability.^{1,10,11} To address the question of stability in a rational manner, the degradation mechanisms of the systems need to be understood and considered for the design of new electrocatalyst materials. Degradation of the electrocatalysts in fuel cells—mostly still Pt-based nanoparticles on carbon supports—occurs predominantly under harsh potential fluctuations, particularly during start-up and shut-down (start–stop) cycles where the electrode potential can locally reach values up to 1.5 V.^{12–16} At these high potentials, Pt dissolution, eventually followed by particle growth due to Ostwald ripening (i.e., dissolution of small Pt particles and redeposition of the Pt species from solution at larger particles), might occur.⁹ Furthermore, corrosion of the carbon support, accompanied with the detachment and/or agglomeration of Pt nanoparticles from the support can take

Received: September 10, 2012

Published: November 28, 2012

place.¹⁴ Thus, the catalyst support is one critical target to be optimized in order to improve the durability of the fuel cell.¹⁷ The most widely used approach in this respect is the exchange of the standard carbon black supports for highly graphitized carbon blacks.¹⁸ Although this has shown to increase durability by kinetically delaying the carbon oxidation, the reduction of the carbon surface area upon graphitization leads to a significant decrease in catalyst dispersion and thus also in mass activity. Alternative carbon-free supports like conductive metal oxides, carbides and nitrides have shown promising properties as electrocatalyst supports. However, even if some of these approaches have resulted in improved stabilities, the low conductivity of most of these materials strongly reduces their performance.^{19–21}

Nanostructuring of support materials offers the possibility of controlling and improving several properties at the same time. Recently, several new nanostructured carbon supports, like colloid-imprinted carbon (CIC) supports,²² ordered hierarchical nanostructured carbon (OHNC),²³ carbon nanotubes (CNTs)²⁴ and multi walled carbon nanotubes (MWCNTs),²⁵ ordered mesoporous carbons CMK-3,²⁶ carbon shells^{27–29} and microemulsion-templated carbons^{30,31} have been introduced as alternatives of catalyst supports for low temperature fuel cells. Although the benefits of nanostructured supports for improving catalyst dispersion, and therefore improved catalyst utilization, are generally suggested, the stability and durability of Pt catalysts supported on these kinds of materials, particularly under start–stop conditions, are less studied. The specific approach pursued by us relies on the synthesis of designed nanostructured graphitic carbon materials, which besides providing high porosity for facile mass transfer and high conductivity, exhibit at the same time a defined mesoporous structure for the stabilization of the Pt nanoparticles by pore confinement. The design of the tailored mesoporous structure, as present in Hollow Graphitic Spheres (HGS), is based on three key elements:

- high surface area ($>1000 \text{ m}^2 \text{ g}^{-1}$) in order to provide good dispersion,
- high degree of graphitization in order to reduce carbon corrosion issues,³² and
- interconnected pore system with a narrow pore size distribution so that Pt nanoparticles can be encapsulated and thus stabilized.

The pore confinement anchors the Pt nanoparticles on the support material (Figure 1), in spite of the substantial morphological changes brought about by the detrimental potential fluctuations during operation. Degradation in a fuel cell by particle detachment and agglomeration of the particles is thus significantly suppressed.

EXPERIMENTAL SECTION

Synthesis of Hollow Graphitic Spheres (HGS) and Pt@HGS.

The synthesis of the silica exotemplate was carried out as reported elsewhere.³³ The detailed synthesis procedure is described in the Supporting Information. A typical synthesis route for HGS is as follows: 1 g of the silica exotemplate material (with a total pore volume of $0.37 \text{ cm}^3 \text{ g}^{-1}$ determined by N_2 physisorption) is impregnated twice with an ethanolic solution of iron(III) nitrate nonahydrate $\text{Fe}(\text{NO}_3)_3 \cdot 9\text{H}_2\text{O}$ 2 M (0.37 mL each). The slurry is dried for 12 h at 75 °C. Prior to the impregnation of the polymer precursor, the silica exotemplate/catalyst material is evacuated under vacuum for 1 h. Afterward, a mixture of 0.37 mL of divinylbenzene (DVB) and 0.05 g of azo-bis-(isobutyronitrile) (AIBN) is incorporated into the

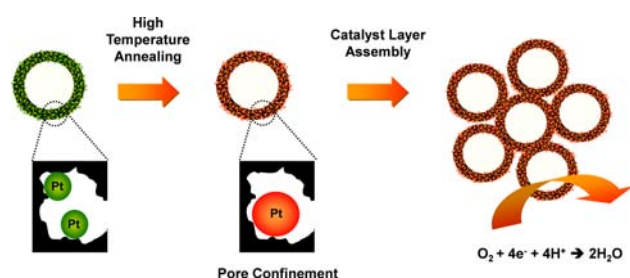


Figure 1. Schematic model of Pt encapsulation by pore confinement. Presynthesized HGS is impregnated with a Pt salt precursor under ultrasonication. After a reduction step under 30% H_2 in Ar at 250 °C, Pt nanoparticles smaller than 2 nm are formed. A high temperature annealing step up to 900 °C leads to the growth and subsequent confinement of Pt nanoparticles of ca. 3–4 nm in the mesoporous structure of the HGS.

mesopores of the silica exotemplate via the incipient wetness method under Ar. The resulting material is heated at 75 °C for 24 h to complete the polymerization of DVB under Ar. The carbonization of the poly(divinylbenzene) (PDVB) in the mesopores is achieved by thermal treatment to 1000 °C (heating rate of $5 \text{ }^\circ\text{C min}^{-1}$) for 4 h under nitrogen flow. The silica exotemplate is dissolved by using HF 10 vol.% in water during 6 h. After washing the remaining HF with water, the material is treated with an excess of concentrated HCl to remove the Fe. The material is washed four times with Millipore water and once with ethanol. The washing process is carried out by centrifugation (14 000 rpm, 5 min) and redispersion assisted by ultrasonication (5 min). Finally, the material is dried at 75 °C overnight.

Pt nanoparticles supported on HGS (20 wt %) were synthesized via ultrasound assisted incipient wetness impregnation of hexachloroplatinic acid ($\text{H}_2\text{PtCl}_6 \cdot x\text{H}_2\text{O}$) solution in ethanol and further gas phase reduction under H_2/Ar atmosphere at 250 °C for 3 h. Typically, the exact amount of $\text{H}_2\text{PtCl}_6 \cdot x\text{H}_2\text{O}$ precursor corresponding to a theoretical 20 wt % of Pt content in the final material is dissolved in a volume of ethanol equivalent to the pore volume of the HGS (measured by N_2 physisorption). For 100 mg of HGS with a total pore volume of $1.7 \text{ cm}^3 \text{ g}^{-1}$, 66 mg of $\text{H}_2\text{PtCl}_6 \cdot x\text{H}_2\text{O}$ are dissolved in 0.17 mL of ethanol. The resulting solution is impregnated onto the HGS support, and the resulting composite is further ultrasonicated for 30 min. Subsequently, the ethanol is evaporated under Ar flow at 100 °C during 1 h in a glass tube furnace. Afterward, the reduction step is carried out in the same glass tube furnace using a mixture of 30 vol % H_2 in Ar. The sample is then heated to 250 °C with a rate of $2.5 \text{ }^\circ\text{C min}^{-1}$ and kept at this temperature for 3 h. After the reduction is finished, the H_2 flow is turned off and the material is annealed at high temperature with a rate of $5 \text{ }^\circ\text{C min}^{-1}$ under Ar. Pt@HGS for *ex situ* electrochemical measurements was annealed at 900 °C and for the *in situ* fuel cell characterization to 850 °C. This temperature difference results in a particle size difference of $<1 \text{ nm}$. Material characterization methods are fully described in the Supporting Information.

Ex Situ Half Cell Electrochemical Measurements. *Ex situ* electrochemical measurements were conducted at room temperature in a Teflon three-compartment electrochemical cell, using a rotating disk electrode (RDE) setup. Details on catalysts suspensions and film preparation, instrumentation, experiment parameters and activity determination can be found in the Supporting Information. The *ex situ* aging tests consisted of 10 800 potential cycles (triangular wave) between 0.4 and 1.4 V_{RHE} with a sweep rate of 1 V s^{-1} . Cleaning of the catalyst surface was not performed before starting the degradation test, in order to follow the changes of the Pt surface area from the beginning. CO-stripping was used to monitor the real Pt surface area in cm^2 after 0, 360, 1080, 2160, 3600, 5400, 7200, and 10 800 potential cycles. The tests for Pt/Vulcan as well as Pt@HGS were performed with an identical loading of catalyst (i.e., mass of Pt per surface area) at the working electrode, namely, $30 \mu\text{g}_{\text{Pt}} \text{ cm}^{-2}$.

In Situ Fuel Cell Measurements. *In situ* electrochemical degradation was investigated by single cell measurements. Electrodes

were prepared by hot spraying of the respective catalyst dispersions in a mixture of deionized-water/2-propanol (70:30), using an ultrasonic atomizing nozzle system (Sono-Tek). Commercial Pt/Carbon (40wt. %, Johnson Matthey) was used as anode electrocatalyst. Pt@HGS (20 wt %) and the in-house prepared Pt/Vulcan (20 wt %) were used as cathode electrocatalysts. The catalyst loadings were $0.18 \text{ mg}_{\text{Pt}} \text{ cm}^{-2}$ at the anode and $0.36 \text{ mg}_{\text{Pt}} \text{ cm}^{-2}$ at the cathode. Membrane Electrode Assemblies (MEAs) were fabricated by hot pressing ($140 \text{ }^\circ\text{C}$, 10 kN, 10 min) of commercial Nafion NR212 ($50 \text{ }\mu\text{m}$) membranes in between of the anode and cathode. After the single cell assembly (active area: 50 cm^2 , water cooled hardware) and 2 h of galvanostatic activation (manually adjusting to maximum current densities keeping the cell voltage always above 300 mV), the fuel cell performance tests were carried out at $80 \text{ }^\circ\text{C}$, with a gas pressure of 1 bar (absolute pressure) at both sides, with a 1.5 anode (H_2) and a 2.5 cathode (air) stoichiometry, and relative humidities of 70% at the anode side and 90% at the cathode side (both values related to $80 \text{ }^\circ\text{C}$). The *in situ* aging test consisted of a total of 1000 degradation cycles. The first 500 degradation cycles were performed between 0.4 and 1.4 V with a scan rate of 1 V s^{-1} , and the final 500 degradation cycles between 0.05 and 1.4 V with a scan rate of 1 V s^{-1} . Within the first 500 degradation cycles, standard performance curves were measured every 100 cycles and a final performance curve was recorded after the finalization of the 1000 cycles.

IL-TEM and IL-SEM/STEM Measurements. The catalyst suspensions of Pt@HGS and Pt/Vulcan for the stability tests were diluted by a factor of about 1:5 with ultrapure water. Five microliters of the diluted suspension was loaded at the top side of a gold finder grid (NHA7, Plano) coated with a carbon film (Quantifoil R2/2). To avoid high catalyst loadings, which can result in overlapping catalyst particles, the drop was absorbed off the grid with a tissue after a few seconds. The grid with the Pt/Vulcan reference catalyst was dried and investigated with a standard IL-TEM experiment with a JEM-2200FS (Jeol, Japan) transmission electron microscope, operated at an acceleration voltage of 200 kV. A more extended investigation was carried out with the Pt@HGS material. To obtain surface as well as bulk information, a combined IL-SEM and IL-STEM experiment of the Pt@HGS catalyst was performed with a Hitachi S-5500 ultra-high resolution cold field emission scanning electron microscope at 30 kV, which allows SEM as well as STEM measurements. The electrochemical setup, which was used for *ex situ* half cell stability and activity tests, was also employed for the aging procedure in all IL-TEM and SEM/STEM tests. Positive feedback IR compensation was performed accordingly. The catalyst deposited on the TEM grid was treated electrochemically by immobilizing the gold finder grid on the glassy carbon disc working electrode with the help of a Teflon cap as reported previously.¹⁴ The experiment was designed analogous to the macroscopic degradation study. A total of 3600 degradation cycles between 0.4 and $1.4 \text{ V}_{\text{RHE}}$ with a sweep rate of 1 V s^{-1} without rotation was applied in 0.1 M HClO_4 saturated with argon. No CO-stripping experiments were carried out between the degradation cycles for the identical location studies, because it is not possible to determine the area of such low amounts of catalyst as dispersed on the TEM finder grid. Images were taken after 0 and after 3600 degradation cycles of identical catalyst locations. Additionally to the IL-TEM test for Pt/Vulcan and the IL-SEM/STEM degradation tests for Pt@HGS after 3600 cycles, further IL-TEM investigations were carried out for both materials in the pristine state and after 5000 degradation cycles. All particle size distributions were determined from the 2D IL-TEM and IL-STEM images. As the particles are not spherical, the shape was approximated with ellipses. A diameter corresponding to an ideal sphere was calculated for every single particle from the area obtained from the ellipse, and this was used to calculate the average spherical diameter. Further information regarding the basic IL-TEM method can be found in the literature.^{34–36}

RESULTS AND DISCUSSION

The HGS base material was synthesized using a nanocasting strategy in order to produce highly defined pore structures.³⁷

Additionally, a low temperature graphitization step at temperatures of up to $1000 \text{ }^\circ\text{C}$ was introduced, using transition metal salts as graphitization catalysts.^{38–40} After the graphitization/nanocasting process, the HGS are composed of graphitic domains randomly distributed in an amorphous carbon skeleton, as evidenced in the carbon structure analysis by high resolution transmission electron microscopy (HR-TEM) (Figure 2a). The powder X-ray diffraction patterns (XRD)

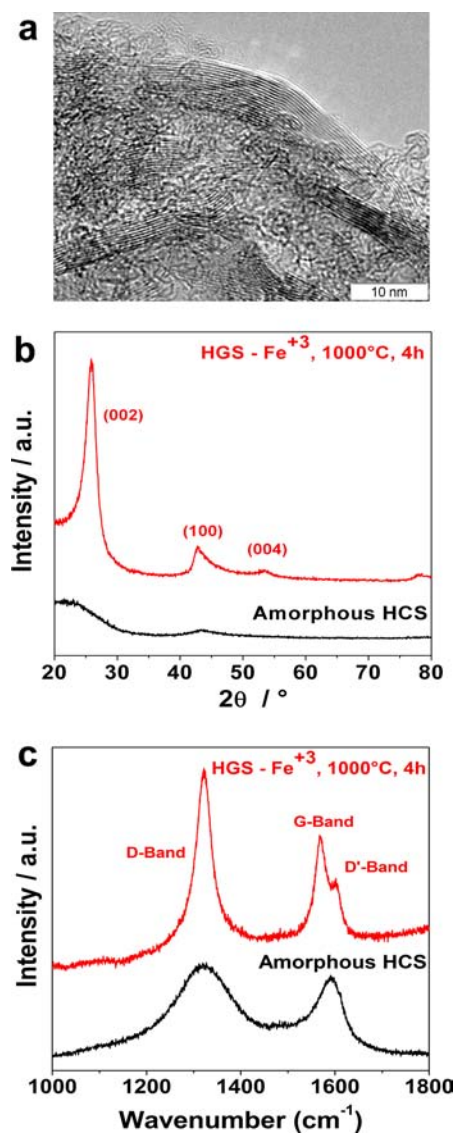


Figure 2. HGS properties after graphitization process using Fe^{3+} as catalyst and comparison to the corresponding material synthesized without graphitization catalyst referred to as Hollow Carbon Spheres (HCS): (a) high-resolution transmission electron micrograph of HGS shell; (b) XRD diffraction patterns of amorphous HCS and HGS; (c) Raman spectra of HCS and HGS.

(Figure 2b) clearly present the (002) reflection at $2\theta = 26.5^\circ$, corresponding to the graphitic domains. Raman spectroscopy confirms that the bulk structure of HGS is composed of two different carbon phases (Figure 2c), in agreement with the results of the HR-TEM analysis. Amorphous hollow carbon spheres present two broad bands centered at 1320 cm^{-1} and 1590 cm^{-1} , which correspond to low order states of the sp^3 (D-band) and sp^2 (G-band) configurations of the carbon atoms,

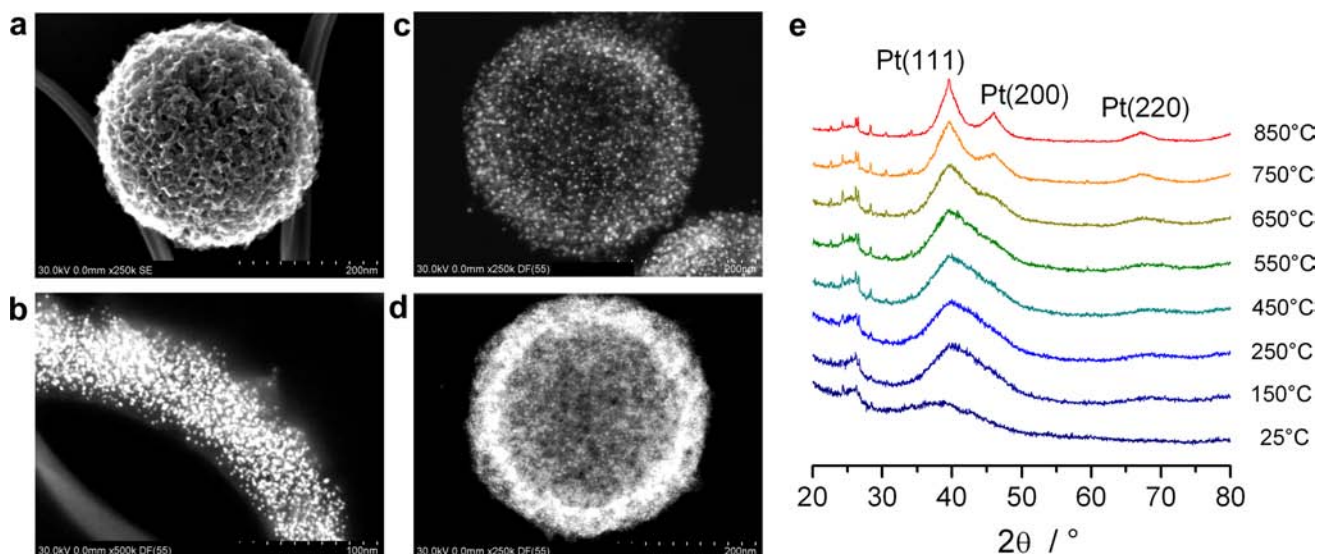


Figure 3. Pore confinement of Pt nanoparticles investigated by *in situ* XRD and DF-STEM: (a) representative high-resolution scanning electron micrograph of HGS support; (b) DF-STEM of a cross-sectional cutting of Pt@HGS (20 wt %) after thermal treatment at 850 °C; (c) DF-STEM of Pt@HGS (20 wt %) after *in situ* XRD to 850 °C; (d) Pt@HGS (20 wt %) without thermal treatment; (e) *in situ* XRD of Pt@HGS (20 wt %): *in situ* XRD collected in reflection geometry. Pt@HGS was heated in the *in situ* XRD chamber under nitrogen atmosphere, heating rate of 2 °C min⁻¹ to 850 °C with intervals of 50 °C, and 30 min stabilization per temperature.

respectively. After the graphitization process with Fe³⁺, not only do both bands become sharper, but also the G band is split into two bands centered at 1570 and 1600 cm⁻¹. The band centered at 1570 cm⁻¹ corresponds to the G-band of highly graphitic domains, while the band centered at 1600 cm⁻¹ is associated to a defect structure of graphite (D'-band).⁴¹ Thermogravimetric analysis (TGA) shows that HGS present two different decomposition temperatures at 600 °C and 700–750 °C in air, corresponding to amorphous carbon and graphitic carbon domains, respectively. The graphitic carbon content deduced from TGA analysis is ca. 40 wt % (Supporting Information Figure 1). The morphological characteristics of HGS can be observed in the high resolution scanning electron micrograph (HR-SEM) in Figure 3a. Nitrogen physisorption measurements demonstrated that the HGS material presents a well developed mesoporous structure as can be observed in the Supporting Information Figure 2. The HGS have a three-dimensional interconnected mesopore system that serves to provide defined hosting sites for Pt nanoparticles. The pore system is characterized by a surface area and a pore volume of approximately 1200 m² g⁻¹ and 1.7 cm³ g⁻¹, respectively. HGS present a uniform and narrow bimodal mesopore size distribution with a major population of pores centered at ca. 3 to 4 nm and a smaller fraction with sizes of ca. 8–10 nm (Supporting Information Figure 3). These distinctive textural properties of HGS make them excellent candidates as high performance support materials.

The crucial Pt encapsulation was possible by a controlled growth process of the nanoparticles inside the pore structure of the HGS. Pt nanoparticles were deposited via ultrasound-assisted incipient-wetness-impregnation, followed by a gas phase reduction with H₂. This method has the advantage, over the conventional wet chemical methods, that after reduction there is only a minor population of particles at the external surface of the support. Pt loading can be tuned with successful pore confinement up to 40 wt %; however, in this work, only 20 wt % Pt loaded catalysts will be discussed. After the reduction process, Pt nanoparticles smaller than 2 nm are

homogeneously distributed within the mesopores. For controlled growth of the Pt particles, the materials are thermally treated under protecting atmosphere.

The thermally induced growth of Pt nanoparticles was monitored by *in situ* XRD, and the initial and final materials were analyzed by dark-field scanning transmission electron microscopy (DF-STEM) (Figure 3). In the *in situ* XRD pattern recorded at 25 °C, it is not possible to identify reflections corresponding to Pt, due to the small particle size. Once the material is heated up to 150 °C, a broad reflection at ca. 40° becomes visible and stays almost unaffected up to 650 °C. At 750 and 850 °C, the powder XRD pattern exhibits typical (111), (200), and (220) reflections corresponding to the face-centered cubic (fcc) Pt crystal structure. Figure 3d shows a representative DF-STEM image of the starting Pt@HGS material and Figure 3c corresponds to the thermally treated material after *in situ* XRD at 850 °C. After the thermal treatment, the density of the Pt nanoparticles in Pt@HGS is decreased, while the particle size is increased from <2 nm to 3–4 nm. Particle size distributions can be found in Supporting Information, Figure 4. The controlled particle growth is promoted by sintering of Pt nanoparticles located in the same pore. Crystallite migration takes place at the Tammann temperature ($T_{\text{Tammann}} = 0.5T_m$; T_m represents the melting point) of Pt at ca. 1023 K (750 °C), which is, however, significantly reduced in the case of small nanoparticles.⁴² Once particle sizes reach 3–4 nm (the pore size determined by nitrogen adsorption), they cannot easily migrate out of the pore because of their confinement. Thus, the final Pt particle size is closely related to the pore diameter of the carbon support. DF-STEM of a cross-sectional cutting of Pt@HGS (Figure 3b) gives strong indications that after the thermal treatment the nanoparticles are successfully confined in the pores of the mesoporous network, rather than being situated in- or outside the carbon shell. Note that in the following the term “Pt@HGS” always refers to these high temperature treated materials.

The outstanding thermal stability of Pt@HGS suggests already that the confinement of the Pt nanoparticles may

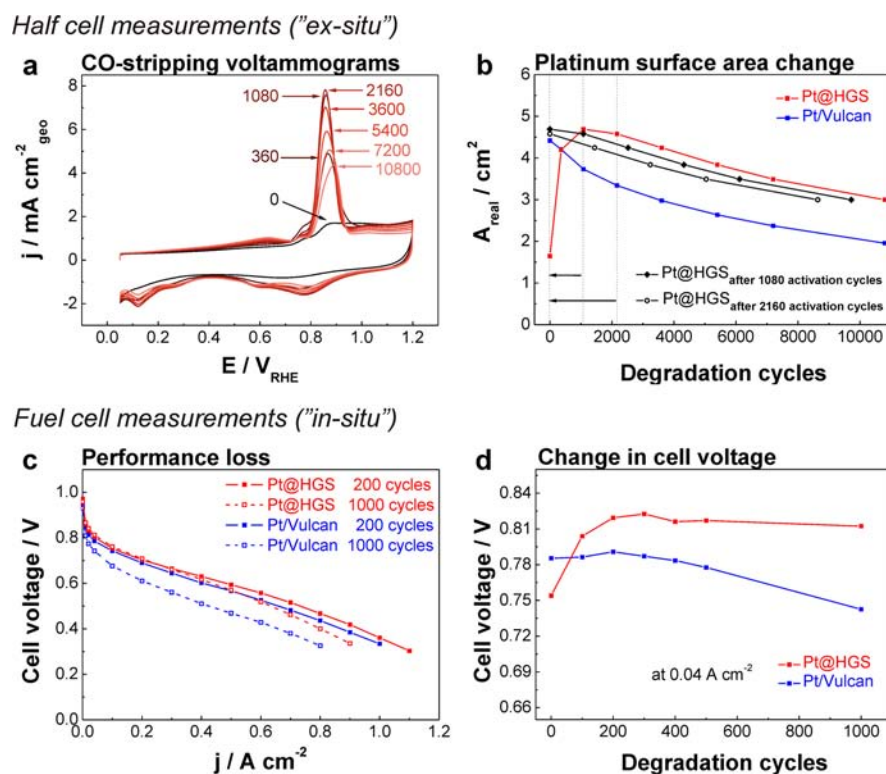


Figure 4. Electrochemical stability tests under *ex situ* (a and b) and *in situ* (c and d) start–stop conditions: (a) CO-stripping voltammograms of Pt@HGS with increasing number of degradation cycles (0, 360, 1080, 2160, 3600, 5400, 7200, 10 800) between 0.4 and 1.4 V_{RHE} with a scan rate of 1 V s^{-1} in argon saturated 0.1 M HClO_4 at $25 \text{ }^\circ\text{C}$, recorded with a sweep rate of 0.05 V s^{-1} . (b) Comparison of Pt surface area change for Pt@HGS and Pt/Vulcan during the *ex situ* degradation test (with $30 \mu\text{g}_{\text{Pt}} \text{ cm}^{-2}$ Pt at working electrode for each catalyst). (c) Fuel cell performance curves (i.e., plot of cell voltage versus current density) at $80 \text{ }^\circ\text{C}$ before and after degradation test under start–stop conditions. (d) Comparison of cell voltage change in the kinetic region for Pt@HGS and Pt/Vulcan during the *in situ* degradation tests at 0.04 A cm^{-2} (with 0.18 and $0.36 \text{ mg}_{\text{Pt}} \text{ cm}^{-2}$ loading at anode and cathode, respectively, for each catalyst).

induce interesting properties to this material. Therefore, we extensively investigated the electrochemical stability of the catalyst under simulated start–stop conditions of a PEM fuel cell. However, first the catalyst activity toward ORR was assessed in order to verify that the material meets the activity requirements for application in a fuel cell. The performance of the Pt@HGS catalyst was investigated by *ex situ* rotating disc electrode (RDE) measurements. After activation, the Pt@HGS catalyst features an electrochemical surface area (ECSA) of $75 \pm 11 \text{ m}^2 \text{ g}^{-1}_{\text{Pt}}$, a specific activity (SA) of $0.47 \pm 0.07 \text{ mA cm}^{-2}_{\text{Pt}}$, and a mass activity (MA) of $0.35 \pm 0.09 \text{ A mg}^{-1}_{\text{Pt}}$ at $0.9 \text{ V}_{\text{RHE}}$ and 1600 rpm in 0.1 M HClO_4 , which are values typical for standard catalysts of comparable Pt particle size.^{43–45} For instance, the Pt/Vulcan reference catalyst utilized in this study shows an ECSA of $67 \pm 6 \text{ m}^2 \text{ g}^{-1}_{\text{Pt}}$, a SA of $0.49 \pm 0.06 \text{ mA cm}^{-2}_{\text{Pt}}$ and a MA of $0.32 \pm 0.07 \text{ A mg}^{-1}_{\text{Pt}}$. These results indicate that the support obviously does not affect the intrinsic activity for ORR, and does not impose limitations for the electrolyte accessibility to Pt nanoparticles despite their pore confinement. Thus, this strongly suggests that the catalyst is fully utilized under the applied conditions.

A first estimation of the catalyst stability was also obtained *ex situ* in the RDE setup by simulating harmful, repeated start–stop cycles. This accelerated degradation test leads to a decay in active surface area of electrocatalysts, which is monitored in between the degradation cycles by CO-stripping measurements.⁴⁶ Figure 4a shows the CO-stripping voltammograms for Pt@HGS with increasing number of degradation cycles. Figure 4b shows the change of Pt surface area in cm^2 of the Pt@HGS

catalyst. Remarkably, the surface area of the catalyst is very low at the beginning, and increases rapidly during the first degradation cycles. This clearly demonstrates that the catalyst requires activation. The activation is most likely due to a burning off of carbon from the platinum surface. Furthermore an oxidation of carbon, which is blocking pores (especially in proximity to platinum particles) might improve accessibility. In addition to this, it is also possible that an improved wetting of the carbon channels in the porous network, as a consequence of the carbon oxidation, might result in a better access to the Pt nanoparticles. However, already after 360 out of 10 800 degradation cycles, a large fraction of the Pt surface is accessible and a maximum in active surface area was obtained after about 1080 degradation cycles. With further increasing the number of degradation cycles, the Pt surface area slowly decreases due to the degradation of the material.

The particle size and Pt loading can have a decisive influence on the degradation rate of a fuel cell catalyst.^{44,47,48} Because of this, we synthesized a Pt/Vulcan reference catalyst (3.6 nm, 20wt.%) with a comparable Pt loading and particle size as the Pt@HGS catalyst. Vulcan XC72R was chosen as comparison support because it easily allows obtaining highly dispersed catalyst, opposite of using highly graphitic commercial supports that present typically lower surface areas, hampering the Pt dispersion and consequently leading to increased particle size. The surface area loss of the Pt/Vulcan material under identical test conditions is shown in Figure 4b. For both materials, the same loading of catalyst ($30 \mu\text{g}_{\text{Pt}} \text{ cm}^{-2}$) was used. The comparable particle size and platinum content are directly

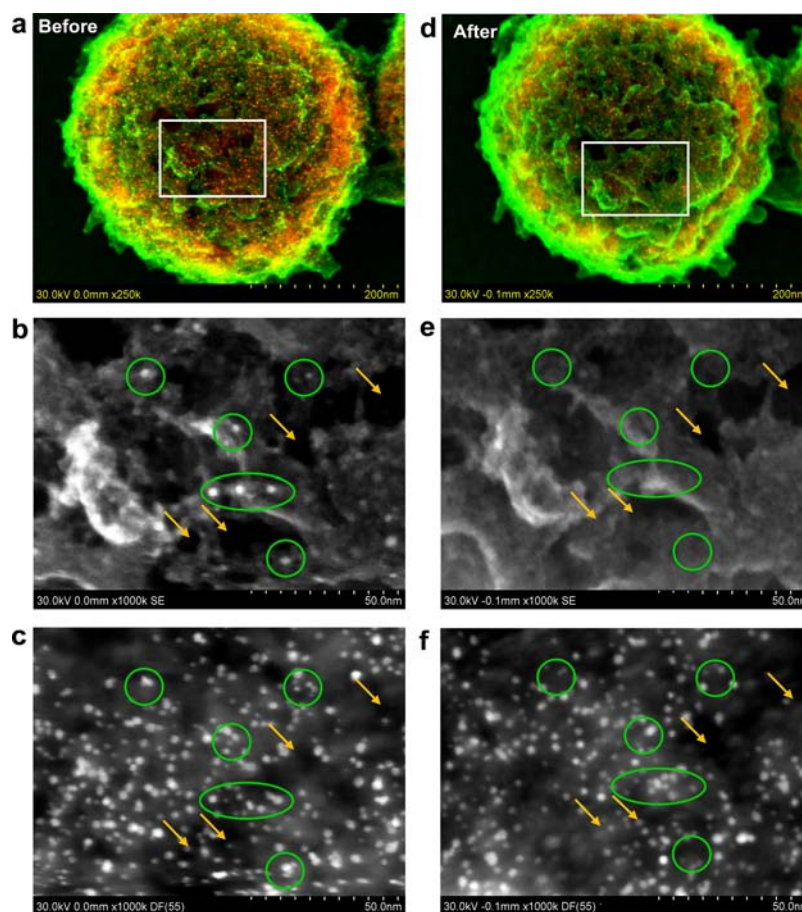


Figure 5. IL-SEM/STEM micrographs of Pt@HGS after 0 and after 3600 electrochemical degradation cycles: (a) overlapping of HR-SEM (green) and DF-STEM (red) of a representative Pt@HGS particle; (b) HR-SEM of a region in the middle of the Pt@HGS particle highlighted with a white square; (c) simultaneously taken DF-STEM micrograph; (d-f) corresponding to identical locations after electrochemical degradation. Yellow arrows point at pores and green circles at Pt nanoparticles placed at the external surface of the HGS support.

reflected in the almost identical maximal surface area of both catalyst materials. After an activation period of 360 cycles, a substantially better stability of high Pt surface areas for the Pt@HGS catalyst compared to Pt/Vulcan becomes obvious. The increased surface area is preserved over the whole degradation investigation, which corresponds to an enhanced lifetime and power output. This is also the case if the Pt@HGS catalyst is first subjected to 1080 (or even after 2160) activating cycles and then in its activated state is compared to the pristine Pt/Vulcan reference material. Such comparison reveals that the Pt@HGS catalyst suffers from a significantly smaller decay in platinum surface area, especially during the first 3000 to 4000 degradation cycles after activation. In the later stage of the degradation test, the slope of the degradation curves becomes almost parallel, indicating similar degradation behavior at this stage of the degradation process. This behavior might indicate comparable dissolution rates of both catalysts, as expected from the commensurable particle size. After the degradation test, no change in specific activity was observed, that is, losses in overall mass activity are determined by the observed decrease in ECSA. After 10 800 degradation cycles, Pt@HGS shows an ECSA of $53 \pm 8 \text{ m}^2 \text{ g}^{-1}_{\text{Pt}}$, a SA of $0.47 \pm 0.07 \text{ mA cm}^{-2}_{\text{Pt}}$ and a MA of $0.25 \pm 0.06 \text{ A mg}^{-1}_{\text{Pt}}$.

Ex situ experiments are powerful to study catalyst stability under well-defined conditions; however, they cannot replace the final testing in a real fuel cell. Therefore, we performed *in situ* degradation measurements in a H_2 -PEMFC single cell.

Fuel cell performance and stability were explored at 80°C for several—to ensure reproducibility—membrane electrode assemblies (MEAs) fabricated from Pt@HGS and Pt/Vulcan as cathode catalysts ($20 \text{ wt } \%$, $0.36 \text{ mg}_{\text{Pt}} \text{ cm}^{-2}$), a commercial Pt/Vulcan as anode catalyst ($40 \text{ wt } \%$, $0.18 \text{ mg}_{\text{Pt}} \text{ cm}^{-2}$) and a NafionNR212 membrane ($50 \mu\text{m}$) used as the proton conductor inside the MEA. Figure 4c displays the performance curves of the Pt@HGS and Pt/Vulcan after 200 start–stop cycles up to 1.4 V, after which the surface is considered to be completely cleaned, and after 1000 start–stop degradation cycles. After 200 cycles, the performance of Pt@HGS is only slightly better than Pt/Vulcan; however, after 1000 cycles, a clear difference in performance becomes obvious.

The comparability of the performance curves of Pt@HGS and Pt/Vulcan after 200 cycles, as well as the *ex situ* measurements, suggests that the Pt catalyst is fully utilized in the Pt@HGS material giving strong indications that there are no limitations for the ionomer access though the mesoporous structure. Pt/Vulcan presents a severe drop in cell voltage after *in situ* degradation, while in the case of Pt@HGS, only slight cell voltage losses become visible at high current densities. This is explicitly represented in Figure 4d, which shows the changes in cell voltage as a function of the number of degradation cycles exclusively in the kinetic region. In the case of Pt/Vulcan, the cell voltage gradually decreases and results in an overall loss of about 50 mV after 1000 start–stop cycles. This is furthermore reflected in the complete down shift of the performance curve

after 1000 start–stop cycles in Figure 4c. In the case of Pt@HGS, the cell voltage remains almost unaffected and significantly higher than in the case of Pt/Vulcan. Moreover, for Pt@HGS, small losses in the overall cell potential are only observed at high current densities. The *in situ* tests are in good agreement with the *ex situ* measurements, where also the initial activity of the Pt/Vulcan and Pt@HGS catalysts after activation are comparable. Moreover, both *ex situ* and *in situ* investigations demonstrated that the design of Pt@HGS leads to significant improvement of catalyst stability, without imposing restrictions on catalyst activity.

Electrochemical data provide integral information on performance of an electrocatalyst. However, in order to understand the reasons for improved properties and for knowledge-based development of better systems, microscopic information is required. Previous work on identical-location transmission electron microscopy (IL-TEM) and identical-location tomography (IL-tomography), which allows comparing identical catalyst locations before and after electrochemical treatment, has demonstrated the potential of these methods for the understanding of the degradation mechanisms occurring on the nanoscale.^{14,34–36,49} To visualize the complex changes occurring to Pt@HGS catalysts, we extended the standard IL-TEM to identical-location scanning electron microscopy/scanning transmission electron microscopy (IL-SEM/STEM) as a complementary methodology.

We used a HR-SEM microscope equipped with a secondary Duo-STEM Bright Field/Dark Field detector that allows simultaneous imaging of surface morphologies in scan mode, and dark field/bright field imaging in transmission mode. Thus, STEM provides information about the changes of the Pt nanoparticles, and HR-SEM allows monitoring the bulk changes associated with the support morphology. Figure 5 shows representative IL-SEM/STEM images of Pt@HGS before and after 3600 degradation cycles. Panels a and d of Figure 5 are overlapped images of the corresponding HR-SEM and DF-STEM micrographs highlighted with green and red colors, respectively. Panels b and e of Figure 5 are high magnification HR-SEM images and panels c and f of Figure 5 are the corresponding DF-STEM images of the marked sections in panels a and d. Representative features of the surface and pore structure of HGS can be seen in Figure 5b,e. Particularly, yellow arrows point at pores and green circles at Pt nanoparticles placed at the external surface of the HGS support. After the degradation treatment, the few Pt nanoparticles located at the external surface have vanished, as they are not confined, and thus not protected, in the mesopores of HGS. Pt nanoparticles located in the pore structure are hardly found in the identical locations after the degradation treatment, most probably due to slight differences in the visual angle, although changes in the carbon texture during cycling and corresponding movement of the Pt particles encapsulated in the mesopores can not be excluded. Nevertheless, the high initial particle density throughout the complete mesoporous network (see Figure 5c) is retained at a remarkable extent after the electrochemical degradation test, and the particle size does not change appreciably (see Figure 5f). This behavior is very different from what is observed for the Pt/Vulcan catalyst. The Pt/Vulcan reference material has been investigated recently in more detail and shows an overlap of several degradation mechanisms (agglomeration, detachment, dissolution and carbon corrosion) under the same test conditions.¹⁴ After 3600 degradation cycles, severe particle growth was observed as

the prevailing mechanism in the Pt/Vulcan reference catalyst (see for instance IL-TEM micrographs in Supporting Information Figure 6). Several indications attributing the observed particle growth to agglomeration were found.¹⁴

A more quantitative evaluation is provided in Figure 6, which compares the particle size distributions of a typical identical

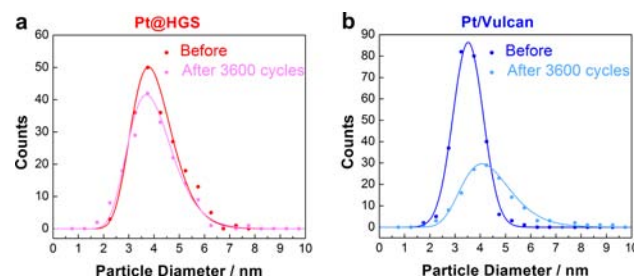


Figure 6. Particle size distributions at a typical catalyst identical location for (a) the Pt@HGS catalyst and (b) the Pt/Vulcan reference catalyst, before and after 3600 degradation cycles between 0.4 and 1.4 V_{RHE} with a scan rate of 1 V s^{-1} in argon saturated 0.1 M HClO_4 at 25°C . The points provide the number of counted particles with the according average spherical diameter, calculated from the area of the particles, while the lines are intended as a guide to the eye.

catalyst location for the Pt/Vulcan and Pt@HGS materials before and after 3600 degradation cycles. It reflects the particle growth for the Pt/Vulcan catalyst, while no increase in average particle size can be observed for the Pt@HGS material. The visual impression of the IL-STEM images (Figure 5c,f) is confirmed: no significant particle growth occurs and only a small loss in the total particle number can be observed. Particularly, after the degradation test, the number of particles in Pt@HGS decreased by only about 14%, while in the case of Pt/Vulcan, it decreased to about half of the original number of particles. In this context, it is remarkable that the number of smaller particles (with a diameter of about 2 nm) slightly increases, which might be an indication for platinum dissolution, where the smaller particle size results from the incomplete dissolution of initial Pt nanoparticles. To further investigate the degradation behavior of both catalysts on the nanoscale also at a later stage of the degradation process, additional IL-TEM experiments of Pt/Vulcan and Pt@HGS were performed, which compare identical catalyst locations in the pristine state and after 5000 degradation cycles. According IL-TEM images and particle size distributions are available in the Supporting Information (Supporting Figures 7–9). IL-TEM results after 5000 degradation cycles again confirm the superior stability of Pt@HGS, which is reflected in a significantly smaller loss in absolute numbers of particles if compared to Pt/Vulcan. Both catalysts suffer from dissolution, but the smaller loss in the absolute number of particles after 5000 cycles for the Pt@HGS (even if compared to Pt/Vulcan after 3600 cycles) points toward reduced detachment. Even more important, the agglomeration for Pt/Vulcan was not observed for the Pt@HGS material to any degree. These observations strongly imply that the Pt particle confinement in the mesopore structure of HGS drastically slows down agglomeration and detachment processes, which are major degradation pathways of the Pt/Vulcan reference catalyst.¹⁴

CONCLUSIONS

Pt nanoparticles were successfully confined within the three-dimensional mesoporous network of HGS. Controlled sintering of Pt nanoparticles during a thermal treatment procedure resulted in a homogeneous particle growth of Pt nanoparticles within the pore system. The remarkable thermal stability of the resulting Pt@HGS material was considered to be a first indication for effective encapsulation. Moreover, the Pt@HGS was extensively studied as cathode catalyst material for low temperature fuel cells. A beneficial effect of the catalyst design on electrochemical stability was predicted from *ex situ* electrochemical degradation tests and verified in a real fuel cell, while no effects of the catalyst design on the activity were observed. Furthermore, advanced IL-TEM and IL-SEM/STEM investigations provided insight into the underlying degradation pathways of the catalyst, and confirmed the positive contribution for stability of the mesoporous carbon network. While Pt@HGS and Pt/Vulcan both suffer from dissolution, the improved preservation of platinum surface area over the course of several thousand degradation cycles for the Pt@HGS material can be explained with the reduction of degradation mechanisms such as detachment and agglomeration due to the confinement and good separation of the Pt nanoparticles in the three-dimensional mesopore system of the highly graphitic support. Preliminary data obtained in our laboratories suggest that this concept is not limited to this electrochemical system and pure Pt as a catalyst, but can be extended to heteroatom-doped supports and other metals for various different applications where stability is an issue.

ASSOCIATED CONTENT

Supporting Information

Additional information about the synthesis and characterization of the materials; detailed *ex situ* electrochemical characterization; and thermo-gravimetric analysis (TGA) curves, nitrogen physisorption isotherms, BJH pore size distributions, particle size distributions of relevant materials and IL-TEM images before and after electrochemical aging. This material is available free of charge via the Internet at <http://pubs.acs.org>.

AUTHOR INFORMATION

Corresponding Author

mayrhofer@mpie.de; schueth@mpi-muelheim.mpg.de

Author Contributions

[‡]These authors contributed equally.

Notes

The authors declare no competing financial interest.

ACKNOWLEDGMENTS

The authors thank the DFG for the financial support through DFG/AiF-Cluster "Innovative Materialien und Verfahren für MT-PEM-Brennstoffzellen". The Electron Microscopy department at Max-Planck-Institut für Kohlenforschung headed by Dr. C. Lehmann is gratefully acknowledged. Dr. C. Weidenthaler is acknowledged for the *in situ* XRD measurements at Max-Planck-Institut für Kohlenforschung. J.C.M. acknowledges financial support by the Kekulé Fellowship from the Fonds der Chemischen Industrie (FCI).

REFERENCES

(1) Rabis, A.; Rodriguez, P.; Schmidt, T. J. *ACS Catal.* **2012**, *2*, 864.

(2) Shao, Y.; Park, S.; Xiao, J.; Zhang, J.-G.; Wang, Y.; Liu, J. *ACS Catal.* **2012**, *2*, 844.

(3) Greeley, J.; Stephens, I. E. L.; Bondarenko, A. S.; Johansson, T. P.; Hansen, H. A.; Jaramillo, T. F.; Rossmeisl, J.; Chorkendorff, I.; Nørskov, J. K. *Nat. Chem.* **2009**, *1*, 552.

(4) Lefèvre, M.; Proietti, E.; Jaouen, F.; Dodelet, J.-P. *Science* **2009**, *324*, 71.

(5) Stamenkovic, V. R.; Fowler, B.; Mun, B. S.; Wang, G.; Ross, P. N.; Lucas, C. A.; Marković, N. M. *Science* **2007**, *315*, 493.

(6) Strasser, P.; Koh, S.; Anniyev, T.; Greeley, J.; More, K.; Yu, C.; Liu, Z.; Kaya, S.; Nordlund, D.; Ogasawara, H.; Toney, M. F.; Nilsson, A. *Nat. Chem.* **2010**, *2*, 454.

(7) Wang, C.; Markovic, N. M.; Stamenkovic, V. R. *ACS Catal.* **2012**, *2*, 891.

(8) Borup, R.; Meyers, J.; Pivovar, B.; Kim, Y. S.; Mukundan, R.; Garland, N.; Myers, D.; Wilson, M.; Garzon, F.; Wood, D.; Zelenay, P.; More, K.; Stroh, K.; Zawodzinski, T.; Boncella, J.; McGrath, J. E.; Inaba, M.; Miyatake, K.; Hori, M.; Ota, K.; Ogumi, Z.; Miyata, S.; Nishikata, A.; Siroma, Z.; Uchimoto, Y.; Yasuda, K.; Kimijima, K.-i.; Iwashita, N. *Chem. Rev.* **2007**, *107*, 3904.

(9) Shao-Horn, Y.; Sheng, W.; Chen, S.; Ferreira, P.; Holby, E.; Morgan, D. *Top. Catal.* **2007**, *46*, 285.

(10) Gasteiger, H. A.; Kocha, S. S.; Sompalli, B.; Wagner, F. T. *Appl. Catal. B* **2005**, *56*, 9.

(11) Gasteiger, H. A.; Marković, N. M. *Science* **2009**, *324*, 48.

(12) Hartnig, C.; Schmidt, T. J. *J. Power Sources* **2011**, *196*, 5564.

(13) Kinoshita, K.; Lundquist, J. T.; Stonehart, P. *J. Electroanal. Chem. Interfacial Electrochem.* **1973**, *48*, 157.

(14) Meier, J. C.; Galeano, C.; Katsounaros, I.; Topalov, A. A.; Kostka, A.; Schüth, F.; Mayrhofer, K. J. J. *ACS Catal.* **2012**, *2*, 832.

(15) Schmidt, T. J.; Baurmeister, J. *J. Power Sources* **2008**, *176*, 428.

(16) Tang, H.; Qi, Z.; Ramani, M.; Elter, J. F. *J. Power Sources* **2006**, *158*, 1306.

(17) Shrestha, S.; Liu, Y.; Mustain, W. E. *Catal. Rev.—Sci. Eng.* **2011**, *43*, 256.

(18) Yu, P. T.; Gu, W.; Makharia, R.; Wagner, F. T.; Gasteiger, H. A. *ECS Trans.* **2006**, *3*, 797.

(19) Huang, S.-Y.; Ganesan, P.; Popov, B. N. *ACS Catal.* **2012**, *2*, 825.

(20) Lewera, A.; Timperman, L.; Roguska, A.; Alonso-Vante, N. *J. Phys. Chem. C* **2011**, *115*, 20153.

(21) Wang, Y.-J.; Wilkinson, D. P.; Zhang, J. *Chem. Rev.* **2011**, *111*, 7625.

(22) Banham, D.; Feng, F.; Fürstenthaupt, T.; Ye, S.; Briss, V. *J. Mater. Chem.* **2012**, *22*, 7164.

(23) Fang, B.; Kim, J. H.; Kim, M.; Yu, J.-S. *Chem. Mater.* **2009**, *21*, 789.

(24) Li, X.; Hsing, I. M. *Electrochim. Acta* **2006**, *51*, 5250.

(25) Hasché, F.; Oezaslan, M.; Strasser, P. *Phys. Chem. Chem. Phys.* **2010**, *12*, 15251.

(26) Ding, J.; Chan, K.-Y.; Ren, J.; Xiao, F.-s. *Electrochim. Acta* **2005**, *50*, 3131.

(27) Kim, J. H.; Fang, B.; Yoon, S. B.; Yu, J.-S. *Appl. Catal. B* **2009**, *88*, 368.

(28) Fang, B.; Kim, J. H.; Kim, M.; Kim, M.; Yu, J.-S. *Phys. Chem. Chem. Phys.* **2009**, *11*, 1380.

(29) Schaefer, Z. L.; Gross, M. L.; Hickner, M. A.; Schaak, R. E. *Angew. Chem., Int. Ed.* **2010**, *49*, 1.

(30) Pylypenko, S.; Olson, T. S.; Carroll, N. J.; Petsev, D. N.; Atanassov, P. *J. Phys. Chem. C* **2010**, *114*, 4200.

(31) Carroll, N. J.; Pylypenko, S.; Atanassov, P. B.; Petsev, D. N. *Langmuir* **2009**, *25*, 13540.

(32) Xia, B. Y.; Wang, J. N.; Teng, S. J.; Wang, X. X. *Chem.—Eur. J.* **2010**, *16*, 8268.

(33) Büchel, G.; Unger, K. K.; Matsumoto, A.; Tsutsumi, K. *Adv. Mater.* **1998**, *10*, 1036.

(34) Mayrhofer, K. J. J.; Ashton, S. J.; Meier, J. C.; Wiberg, G. K. H.; Hanzlik, M.; Arenz, M. *J. Power Sources* **2008**, *185*, 734.

- (35) Mayrhofer, K. J. J.; Meier, J. C.; Ashton, S. J.; Wiberg, G. K. H.; Kraus, F.; Hanzlik, M.; Arenz, M. *Electrochem. Commun.* **2008**, *10*, 1144.
- (36) Meier, J. C.; Katsounaros, I.; Galeano, C.; Bongard, H. J.; Topalov, A. A.; Kostka, A.; Karschin, A.; Schüth, F.; Mayrhofer, K. J. J. *Energy Environ. Sci.* **2012**, *5*, 9319.
- (37) Schüth, F. *Angew. Chem., Int. Ed.* **2003**, *42*, 3604.
- (38) Fuertes, A. B.; Centeno, T. A. *J. Mater. Chem.* **2005**, *15*, 1079.
- (39) Sevilla, M.; Fuertes, A. B. *Carbon* **2006**, *44*, 468.
- (40) Lei, Z.; Xiao, Y.; Dang, L.; Bai, S.; An, L. *Microporous Mesoporous Mater.* **2008**, *109*, 109.
- (41) Tai, F. C.; Wei, C.; Chang, S. H.; Chen, W. S. *J. Raman Spectrosc.* **2010**, *41*, 933.
- (42) Buffat, P.; Borel, J. P. *Phys. Rev. A* **1976**, *13*, 2287.
- (43) Nesselberger, M.; Ashton, S.; Meier, J. C.; Katsounaros, I.; Mayrhofer, K. J. J.; Arenz, M. *J. Am. Chem. Soc.* **2011**, *133*, 17428.
- (44) Sheng, W.; Chen, S.; Vescovo, E.; Shao-Horn, Y. *J. Electrochem. Soc.* **2012**, *159*, B96.
- (45) Ke, K.; Hiroshima, K.; Kamitaka, Y.; Hatanaka, T.; Morimoto, Y. *Electrochim. Acta* **2012**, *72*, 120.
- (46) Mayrhofer, K. J. J.; Arenz, M.; Blizanac, B. B.; Stamenkovic, V.; Ross, P. N.; Markovic, N. M. *Electrochim. Acta* **2005**, *50*, 5144.
- (47) Shao, Y.; Yin, G.; Gao, Y. *J. Power Sources* **2007**, *171*, 558.
- (48) Mench, M. M.; Kumbar, E. C.; Veziroglu, T. N. *Polymer Electrolyte Fuel Cell Degradation*; Academic Press Elsevier: Waltham, 2012.
- (49) Yu, Y.; Xin, H. L.; Hovden, R.; Wang, D.; Rus, E. D.; Mundy, J. A.; Muller, D. A.; Abruña, H. D. *Nano Lett.* **2012**, *12*, 4417.